Quantum phases of multiorbital bosonic gases in a hexagonal lattice

Pengfei Zhang [1], Hui Tan,[1] Jianmin Yuan [2,1] and Yongqiang Li [1,3,*]

[1]*Department of Physics, National University of Defense Technology, Changsha 410073, People's Republic of China*
[2]*Department of Physics, Graduate School of China Academy of Engineering Physics, Beijing 100193, People's Republic of China*
[3]*Hunan Key Laboratory of Extreme Matter and Applications, National University of Defense Technology,*
Changsha 410073, People's Republic of China

Orbital degree of freedom plays an important role for understanding quantum many-body phenomena. In this paper, we study an experimentally related setup with ultracold bosons loaded into hybridized bands of two-dimensional hexagonal optical lattices. We find that the system supports various quantum many-body phases at zero temperature, including chiral superfluid and chiral Mott insulating phases by breaking time-reversal symmetry, and the time-reversal-even insulating phase, based on dynamical mean-field theory. In the deep insulating regime, the time-reversal-even phase arises from the interplay of effective Dzyaloshinskii-Moriya and Heisenberg exchange interactions. To relate to experimental situations, we make band-structure calculations to obtain the Hubbard parameters, and show that these orbital ordering phases persist also in the presence of next-nearest-neighbor hopping.

I. INTRODUCTION

Quantum simulation plays an important role for understanding difficult quantum problems in physics [1–4], such as quantum magnetism [5] and topological quantum matter [6]. Ultracold gases in optical lattices are one of the most promising and flexible quantum simulators for quantum many-body problems with an unprecedented level of control. Different species or hyperfine states of atoms have been loaded into optical lattices [7,8], which are treated as pseudospin degrees of freedom, and significant efforts have been made to explore magnetic phases in ultracold systems [9–11]. Complex optical lattices, such as triangular [12,13], hexagonal [14,15], Lieb [16], and kagome lattices [17], trigger even more rich physics, as a result of geometric frustration arising when magnetic interactions between adjacent spins on a lattice are incompatible with lattice geometry [18,19].

In addition to spin, an alternative approach towards optical lattice simulators is based on orbital degrees of freedom, which provide an opportunity to investigate new orbital physics [20,21]. Here, higher-Bloch bands can be implemented as orbital degrees of freedom, where p-orbital systems have been explored extensively both in theories [22–29] and experiments [30–33] in recent years. Various interesting phases have been observed, including chiral superfluid [30] and sliding phases [33], where the key element is onsite interactions between atoms for building many-body correlations. Recently, special attention has been paid to the complex-lattice setup, and ultracold ^{87}Rb atoms have been successfully loaded into the s and $p_{x,y}$ bands of a hexagonal lattice [34–36]. In contrast to the square-lattice case [29–31], a special property of this hexagonal system is that it possesses nearly flat

dispersion relations around the K and M points of the first Brillouin zone [37]. Distinct phenomena have been observed experimentally even in the weakly interacting regime, including Potts-nematic superfluid [34] and chiral superfluid phases [35] with bosons condensing at M and K points in the first Brillouin zone, respectively. These experiments indicate that nontrivial underlying mechanics appears for the multiorbital system in a hexagonal lattice, where temperature and interaction may play important roles for understanding these quantum phenomena. Another open question is that it is still unclear how orbital textures adapt to the hexagonal-lattice geometry in the strongly interacting regime.

Motivated by the experiments [34,35,38], we study a bosonic system in a two-dimensional (2D) hexagonal lattice with alternating deep and shallow wells, and focus on emergent phenomena from multiorbital effects and lattice geometries. To explore the physics in the strongly correlated regime, a strong laser is utilized to freeze the motional degrees of freedom of atoms in the third direction. By adjusting the sublattice potential imbalance, the s orbital of the shallow wells can be in resonance with the $p_{x,y}$ orbitals of the deep sites, realizing a multiorbital system with neglecting all the other orbitals. For a sufficiently deep lattice, the system can be described by an extended Bose-Hubbard model. It is expected that various quantum phases appear as a result of the multiorbital interplay in the strongly interacting regime.

To explore the many-body physics of the multiorbital system, we utilize a bosonic version of dynamical mean-field theory (BDMFT) applied within the full range from small to large coupling. With BDMFT, local quantum fluctuations are taken into account to resolve competing long-range orders. To explore various exotic magnetic or superfluid phases which break lattice-translational symmetry, we implement
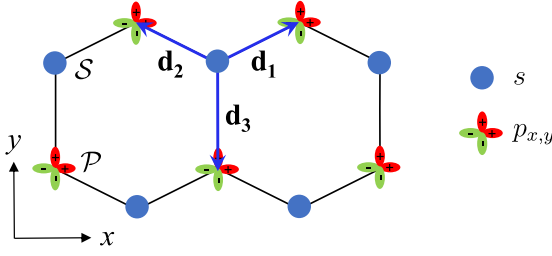
*li_yq@nudt.edu.cn

033314-1

FIG. 1. Setup of the two-dimensional bipartite hexagonal lattice, which possesses two sets of sublattices labeled by $\mathcal{S}$ and $\mathcal{P}$, respectively. By adjusting sublattice potential imbalance, the s- and p-orbital bosons can be loaded to the shallow and deep wells, respectively, as achieved in the experiments [34,35], realizing a multiorbital bosonic system in optical lattices.

real-space BDMFT, where the self-energy and Green's function capture quantum many-body phases with exotic orbital textures. We find that the system supports various quantum many-body phases, including chiral superfluid, chiral Mott insulating, and time-reversal-even insulating phases, based on BDMFT. To explain the underlying mechanics for the time-reversal-even Mott phase, a fourth-order orbital-exchange model is derived. Finally, we make band-structure calcula-

tions to obtain the Hubbard parameters with hopping terms up to next-nearest neighbors, and map out the many-body phase diagram, which is more closely related to the experimental situation.

The paper is organized as follows. In Sec. II, we introduce the system and the model studied here, as well as the theoretical approach. In Sec. III, we present a detailed discussion of many-body properties of the system. We conclude in Sec. IV.

II. MODEL AND METHOD

A. Model

We consider a single-component bosonic gas loaded into a hexagonal lattice consisting of two sublattices, denoted as $\mathcal{S}$ and $\mathcal{P}$. By adjusting sublattice potential imbalance [34,35], a multiorbital system can be realized with $\mathcal{S}$ and $\mathcal{P}$ hosting the s and $p_{x,y}$ orbitals, respectively, as shown in Fig. 1. The corresponding annihilation operators for the s- and $p_{x,y}$-orbital bosonic particles are denoted as $\hat{s}$ and $\hat{p}_{x,y}$, respectively. Here, a strong confinement is added to freeze the motional degrees of freedom in the third direction, realizing a two-dimensional bipartite lattice system. For a sufficiently deep lattice, the system can be described by a generalized Bose-Hubbard model:

$$\hat{H} = t_{sp} \sum_{\mathbf{r} \in \mathcal{S}} \sum_{a=1,2,3} \left[\hat{s}_{\mathbf{r}}^{\dagger}(\vec{\hat{p}}_{\mathbf{r}+\mathbf{d}_a} \cdot \mathbf{e}_a) + \text{H.c.} \right] - \mu_s \sum_{\mathbf{r} \in \mathcal{S}} \hat{n}_{\mathbf{r},s} - \mu_p \sum_{\mathbf{r}' \in \mathcal{P}} \left(\hat{n}_{\mathbf{r}',p_x} + \hat{n}_{\mathbf{r}',p_y} \right) + \frac{U_s}{2} \sum_{\mathbf{r} \in \mathcal{S}} \hat{n}_{\mathbf{r},s}(\hat{n}_{\mathbf{r},s} - 1)$$

$$+ \sum_{\substack{\mathbf{r}' \in \mathcal{P} \\ \sigma=x,y}} \frac{U_{p_\sigma}}{2} \hat{n}_{\mathbf{r}',p_\sigma}\left(\hat{n}_{\mathbf{r}',p_\sigma} - 1 \right) + 2\,U_{p_{xy}} \sum_{\mathbf{r}' \in \mathcal{P}} \hat{n}_{\mathbf{r}',p_x}\hat{n}_{\mathbf{r}',p_y} + J \sum_{\mathbf{r}' \in \mathcal{P}} (\hat{p}_{\mathbf{r}',x}^{\dagger}\hat{p}_{\mathbf{r}',x}^{\dagger}\hat{p}_{\mathbf{r}',y}\hat{p}_{\mathbf{r}',y} + \text{H.c.}), \tag{1}$$

where the unit vectors $\mathbf{e}_1 = (\frac{\sqrt{3}}{2}, \frac{1}{2})$, $\mathbf{e}_2 = (-\frac{\sqrt{3}}{2}, \frac{1}{2})$, $\mathbf{e}_3 = (0, -1)$, and $\mathbf{d}_i = a_0\mathbf{e}_i$ are the relative positions between the two sublattices, with a_0 being the lattice constant. t_{sp} is the hopping amplitude between the $\mathcal{S}$ and $\mathcal{P}$ sublattices, $\vec{\hat{p}}_{\mathbf{r}} = (\hat{p}_{\mathbf{r},x}, \hat{p}_{\mathbf{r},y})$ is the shorthand notation for the annihilation operators $\hat{p}_x$ and $\hat{p}_y$ at site $\mathbf{r}$, and $\hat{n}_{\mathbf{r},\sigma}$ is the number operator for the σ orbital at site $\mathbf{r}$. μ_s and μ_p are the chemical potentials for the s and p orbitals, respectively. U_s, U_{p_x}, U_{p_y}, and $U_{p_{xy}}$ are onsite density-density interactions for the s, p_x, and p_y orbitals, respectively, and J denotes the orbital-changing interaction. According to symmetry analysis, the hexagonal-lattice system possesses $U_{p_x} = U_{p_y}$ and $J = \frac{U_{p_x} - 2U_{p_{xy}}}{2}$ for the p-orbital interaction terms. In the deep lattice limit, the harmonic approximation for a lattice site yields $U_{p_x} = U_{p_y} = 3U_{p_{xy}} = 0.75U_s$ [39]. In this approximation, the last three terms of Eq. (1) can be rewritten as

$$\hat{H}_{\text{int},\mathcal{P}} = \frac{U_{p_x}}{2} \sum_{\mathbf{r} \in \mathcal{P}} \left(\hat{n}_{\mathbf{r},p}^2 - \frac{1}{3}\hat{L}_{z,\mathbf{r}}^2 \right), \tag{2}$$

with the density $\hat{n}_{\mathbf{r},p} = \hat{n}_{\mathbf{r},p_x} + \hat{n}_{\mathbf{r},p_y}$, and the orbital angular momentum $\hat{L}_{z,\mathbf{r}} = i(\hat{p}_{\mathbf{r},x}^{\dagger}\hat{p}_{\mathbf{r},y} - \hat{p}_{\mathbf{r},y}^{\dagger}\hat{p}_{\mathbf{r},x})$ [22].

B. Method

To understand this generalized Bose-Hubbard model, we utilize BDMFT [40,41] to calculate many-body ground states of the system described by Eq. (1). The advantage of dynamical mean-field theory beyond static mean-field theory is that it includes local quantum fluctuations of the strongly correlated system. The key point of BDMFT is to map the many-body lattice system to a single-site problem, which is then solved self-consistently. For exploring various exotic magnetic or superfluid phases which break lattice-translational symmetry, we implement a real-space BDMFT (RBDMFT) [42–46]. Within RBDMFT, the self-energy is taken to be local, but depends on the lattice site, i.e., $\Sigma_{i,j} = \Sigma_i \delta_{ij}$, where δ_{ij} is a Kronecker delta. In RBDMFT, our challenge is to solve the single-site problem, and the physics of site i is given by the local effective action S_{eff}^i, which can be obtained from the standard derivation [47]. Here, we have two sets of sublattices labeled by $\mathcal{S}$ and $\mathcal{P}$, which indicates that we need two types

of the local effective actions $S_{\text{eff}}^{\mathcal{S}}$ and $S_{\text{eff}}^{\mathcal{P}}$:

$$S_{\text{eff}}^{\mathcal{S}} = \int_0^\beta d\tau d\tau' \sum_{\sigma=x,y} \begin{pmatrix} b_{0,s}^*(\tau) \\ b_{0,s}(\tau) \end{pmatrix}^T \mathcal{G}_{0,s,s',p_\sigma,p_\sigma'}^{-1}(\tau-\tau') \begin{pmatrix} b_{0,s'}(\tau') \\ b_{0,s'}^*(\tau') \end{pmatrix}$$

$$+ \int_0^\beta d\tau \left\{ \sum_{\langle 0j\rangle,\sigma=x,y} t^{0j}(b_{0,s}^*(\tau)\phi_{j,p_\sigma}(\tau) + \phi_{j,p_\sigma}^*(\tau)b_{0,s}(\tau)) + \frac{U_s}{2} n_{0,s}(\tau)(n_{0,s}(\tau)-1) \right\}, \tag{3}$$

$$S_{\text{eff}}^{\mathcal{P}} = \int_0^\beta d\tau d\tau' \sum_{\sigma=x,y} \begin{pmatrix} b_{0,p_\sigma}^*(\tau) \\ b_{0,p_\sigma}(\tau) \end{pmatrix}^T \mathcal{G}_{0,p_\sigma,p_\sigma',s,s'}^{-1}(\tau-\tau') \begin{pmatrix} b_{0,p_\sigma'}(\tau') \\ b_{0,p_\sigma'}^*(\tau') \end{pmatrix}$$

$$+ \int_0^\beta d\tau \left\{ \sum_{\langle 0j\rangle,\sigma=x,y} t^{0j}\big(b_{0,p_\sigma}^*(\tau)\phi_{j,s}(\tau) + \phi_{j,s}^*(\tau)b_{0,p_\sigma}(\tau)\big) + 2U_{p_{xy}} n_{0,p_x}(\tau)n_{0,p_y}(\tau) \right.$$

$$\left. + \sum_{\sigma=x,y} \frac{U_{p_\sigma}}{2} n_{0,p_\sigma}(\tau)\big(n_{0,p_\sigma}(\tau)-1\big) + J\big(b_{0,p_x}^*(\tau)b_{0,p_x}^*(\tau)b_{0,p_y}(\tau)b_{0,p_y}(\tau) + \text{H.c.}\big) \right\}, \tag{4}$$

where

$$\mathcal{G}_{0,\nu_1,\nu_1',\nu_2,\nu_2'}^{-1}(\tau-\tau')$$

$$= \begin{pmatrix} (\partial_{\tau'} - \mu_{\nu_1})\delta_{\nu_1,\nu_1'} + \sum_{\langle 0j\rangle,\langle 0j'\rangle} t^{0j}t^{0j'}G_{j,j',\nu_2,\nu_2'}^1(\tau,\tau') & \sum_{\langle 0j\rangle,\langle 0j'\rangle} t^{0j}t^{0j'}G_{j,j',\nu_2,\nu_2'}^2(\tau,\tau') \\ \sum_{\langle 0j\rangle,\langle 0j'\rangle} t^{0j}t^{0j'}G_{j,j',\nu_2,\nu_2'}^{2*}(\tau',\tau) & (-\partial_{\tau'} - \mu_{\nu_1})\delta_{\nu_1,\nu_1'} + \sum_{\langle 0j\rangle,\langle 0j'\rangle} t^{0j}t^{0j'}G_{j,j',\nu_2,\nu_2'}^1(\tau',\tau) \end{pmatrix},$$

with $G_{j,j',\nu_2,\nu_2'}^1(\tau,\tau') = -\langle b_{j,\nu_2}(\tau)b_{j',\nu_2'}^*(\tau')\rangle_0 + \phi_{j,\nu_2}(\tau)\phi_{j',\nu_2'}^*(\tau')$ and $G_{j,j',\nu_2,\nu_2'}^2(\tau,\tau') = -\langle b_{j,\nu_2}(\tau)b_{j',\nu_2'}(\tau')\rangle_0 + \phi_{j,\nu_2}(\tau)\phi_{j',\nu_2'}(\tau')$. Here, $\mathcal{G}_{0,\nu_1,\nu_1',\nu_2,\nu_2'}^{-1}$ is a local noninteracting propagator interpreted as a dynamical Weiss mean field which simulates the effects of all other sites. The static bosonic mean fields are defined as $\phi_{j,\nu}(\tau) = \langle b_{j,\nu}(\tau)\rangle_0$, where $\langle \ldots \rangle_0$ means the expectation value in the cavity system without the impurity site. Note here that we use $\hat{b}_{i,\nu}$ to denote the bosonic annihilation operator for the ν orbital at site i to shorten the notation of the function. Actually, it is difficult to resolve this effective action analytically. In order to obtain many-body ground states, we utilize the Hamiltonian representation and express the effective action in terms of the Anderson impurity Hamiltonian [48,49]:

$$\hat{H}_A^{\mathcal{S}} = \sum_{\langle 0j\rangle,\sigma} t^{0j}(\phi_{j,p_\sigma}^*\hat{b}_{0,s} + \text{H.c.}) + \frac{U_s}{2}\hat{n}_{0,s}(\hat{n}_{0,s}-1) - \mu_s\hat{n}_{0,s} + \sum_l \epsilon_l\hat{a}_l^\dagger\hat{a}_l + \sum_l (V_{l,s}\hat{a}_l^\dagger\hat{b}_{0,s} + W_{l,s}\hat{a}_l\hat{b}_{0,s} + \text{H.c.}), \tag{5}$$

$$\hat{H}_A^{\mathcal{P}} = \sum_{\langle 0j\rangle,\sigma} t^{0j}(\phi_{j,s}^*\hat{b}_{0,p_\sigma} + \text{H.c.}) + \sum_\sigma \left[\frac{U_{p_\sigma}}{2}\hat{n}_{0,p_\sigma}\big(\hat{n}_{0,p_\sigma}-1\big) - \mu_p\hat{n}_{0,p_\sigma} \right] + 2U_{p_{xy}}\hat{n}_{0,p_x}\hat{n}_{0,p_y}$$

$$+ J\big(\hat{b}_{0,p_x}^\dagger\hat{b}_{0,p_x}^\dagger\hat{b}_{0,p_y}\hat{b}_{0,p_y} + \text{H.c.}\big) + \sum_l \epsilon_l\hat{a}_l^\dagger\hat{a}_l + \sum_{l,\sigma} \big(V_{l,\sigma}\hat{a}_l^\dagger\hat{b}_{0,p_\sigma} + W_{l,\sigma}\hat{a}_l\hat{b}_{0,p_\sigma} + \text{H.c.}\big), \tag{6}$$

where the bath of condensed bosons is represented by the Gutzwiller term with $\phi_{j,\nu} = \langle \hat{b}_{j,\nu}\rangle$ for the component ν. The normal bath is described by operators $\hat{a}_l^\dagger$ with energies ϵ_l, where the coupling between the normal bath and impurity site is realized by $V_{l,\sigma}$ and $W_{l,\sigma}$. The l denote the bath orbitals. By diagonalizing the Anderson Hamiltonian in the Fock basis, the corresponding solution of the impurity model can be obtained. The numerical parameters are chosen as follows: the number of bath orbitals is 4, the maximum occupation number for each bath orbital is 2, and the maximum occupation number of bosons per orbital state is 5. After diagonalization, we finally obtain the local Green's functions in the Lehmann

representation:

$$G_{A,\nu\nu'}^1(i\omega_n) = \frac{1}{Z}\sum_{m,n} \langle m|\hat{b}_\nu|n\rangle\langle n|\hat{b}_{\nu'}^\dagger|m\rangle$$

$$\times \frac{e^{-\beta E_n} - e^{-\beta E_m}}{E_n - E_m + i\hbar\omega_n} + \beta\phi_\nu\phi_{\nu'}^*,$$

$$G_{A,\nu\nu'}^2(i\omega_n) = \frac{1}{Z}\sum_{m,n} \langle m|\hat{b}_\nu|n\rangle\langle n|\hat{b}_{\nu'}|m\rangle$$

$$\times \frac{e^{-\beta E_n} - e^{-\beta E_m}}{E_n - E_m + i\hbar\omega_n} + \beta\phi_\nu\phi_{\nu'}, \tag{7}$$

where ω_n denotes Matsubara frequency. Then, the local self-energy for each site can be obtained via the Dyson equation:

$$\Sigma_A(i\omega_n) = \mathcal{G}_A^{-1}(i\omega_n) - G_A^{-1}(i\omega_n), \qquad (8)$$

where $\mathcal{G}_A^{-1}(i\omega_n)$ denotes the noninteracting Weiss Green's function of the Anderson impurity site. In the framework of RBDMFT, we assume that the impurity self-energy $\Sigma_A(i\omega_n)$ coincides with lattice self-energy $\Sigma_{\text{lattice}}(i\omega_n)$. Therefore, we can employ the Dyson equation in real-space representation to compute the interacting lattice Green's function:

$$\mathbf{G}_{\text{lattice}}^{-1}(i\omega_n) = \mathbf{G}_0^{-1}(i\omega_n) - \mathbf{\Sigma}_{\text{lattice}}(i\omega_n), \qquad (9)$$

where the noninteracting lattice Green's function $\mathbf{G}_0^{-1}(i\omega_n) = (i\omega_n\sigma_z + \boldsymbol{\mu}) - \mathbf{t}$, with the matrix of hopping $\mathbf{t}$ determined by lattice structures. Note here that the boldface quantities denote matrices with site-dependent elements [see details in Eq. (A1)]. The self-consistency RBDMFT loop is closed by the Dyson equation to obtain a new local noninteracting propagator. The new Anderson impurity parameters ϵ_l, $V_{l,\sigma}$, and $W_{l,\sigma}$ are then calculated by comparing the old and new Green's functions, and the procedure is then iterated until convergence is reached.

III. RESULTS

A. Many-body phase diagrams

In the first part, we investigate many-body phase diagrams of the bosonic atoms in a 2D hexagonal lattice for different interactions, based on RBDMFT. To distinguish various quantum phases, the superfluid order parameters $\phi_\nu = \frac{1}{N_{\text{lat}}}\sum_i |\langle \hat{b}_{i,\nu}\rangle|$ and local orbital order $\langle \hat{S}_i\rangle = [\langle \hat{S}_i^X\rangle, \langle \hat{S}_i^Y\rangle, \langle \hat{S}_i^Z\rangle]$ are introduced. Here, N_{lat} is the number of lattice sites, and the pseudospin operators from the orbital degrees of freedom are utilized to quantify orbital order, with $\hat{S}_i^X = \frac{1}{2}(\hat{b}_{i,p_x}^\dagger \hat{b}_{i,p_y} + \hat{b}_{i,p_y}^\dagger \hat{b}_{i,p_x})$, $\hat{S}_i^Y = \frac{1}{2i}(\hat{b}_{i,p_x}^\dagger \hat{b}_{i,p_y} - \hat{b}_{i,p_y}^\dagger \hat{b}_{i,p_x})$, and $\hat{S}_i^Z = \frac{1}{2}(\hat{b}_{i,p_x}^\dagger \hat{b}_{i,p_x} - \hat{b}_{i,p_y}^\dagger \hat{b}_{i,p_y})$. Accordingly, we define the structure factor of the real-space orbital textures, $S_{\bar{q}} = |\frac{1}{N_{\text{lat}}}\sum_i \langle \hat{S}_i\rangle e^{i\bar{q}\cdot\bar{r}_i}|$ [50]. To study the multiorbital interplay regime, we choose a special case with the chemical potentials $\mu_s = \mu_p \equiv \mu$, and the interaction strengths $U_{p_x} = U_{p_y} = U_s$. To verify finite-size effects, the largest lattice size $N_{\text{lat}} = 24 \times 24 \times 2$ is chosen in our simulations.

Figure 2 displays the many-body phase diagrams for different orbital-changing interactions $J/U_s = 1/6$ (upper panel) and $J/U_s = -1/6$ (lower panel). As expected, the system favors a superfluid phase for larger hopping, and Mott states develop in the lower hopping regime. As shown in the inset of Fig. 2, we clearly observe a first-order Mott-superfluid phase transition. To examine the effect of a finite number of bath sizes [51], we also calculated the case of five bath orbitals. We find the numerical results remain largely unaffected by including more bath orbitals. A typical feature of the many-body phase diagram is the unusual sequence of lower Mott lobes [2,52], as a result of the multiflavor orbital degrees of freedom. We observe that the phase boundaries for different Mott states are not in the same positions for different sublattices, since the interaction forms of the $\mathcal{S}$ and $\mathcal{P}$ sites are distinct from each
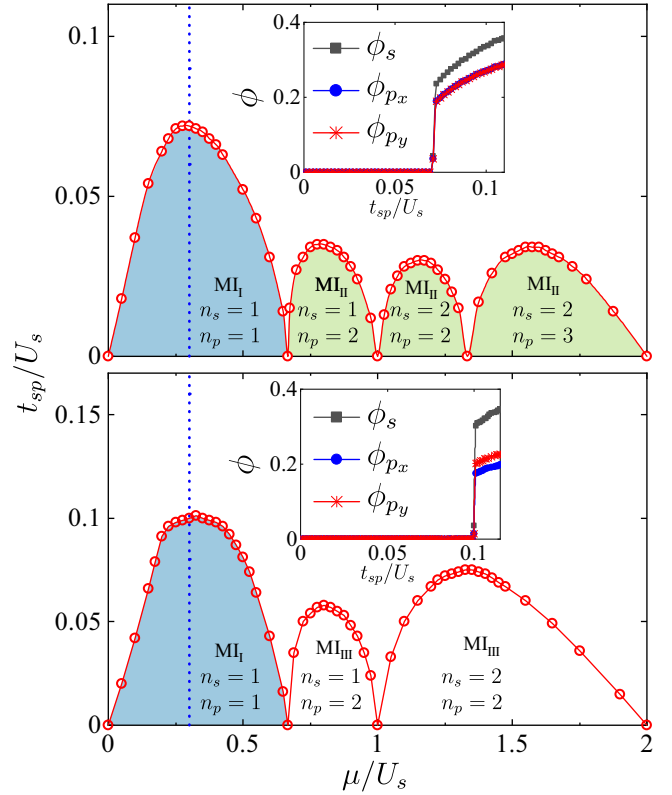

FIG. 2. Phase diagrams of the multiorbital bosonic atoms in a 2D bipartite hexagonal lattice. Insets: Order parameters ϕ_ν are shown as a function of the hopping amplitude t_{sp} for a fixed chemical potential $\mu/U_s = 0.3$ (vertical blue dotted line), indicating a superfluid-Mott insulating phase transition. The chemical potentials are $\mu \equiv \mu_s = \mu_p$, the interaction strengths $U_{p_x}/U_s = U_{p_y}/U_s = 1$, and $J/U_s = 1/6$ (upper) and $J/U_s = -1/6$ (lower).

other. Note here that the case of a bipartite square lattice was also discussed [53].

RBDMFT also resolves long-range orbital order of the many-body phases, since it takes higher-order orbital fluctuations into account in the simulations. We observe orbital-changing-interaction dependent orbital orders. For positive interaction with $J/U_s = 1/6$, we find nonzero orbital angular momentum with $\langle \hat{L}_{z,i}\rangle \neq 0$ both in the superfluid and Mott phases (MI$_{\text{II}}$ with $n > 1$) by breaking time-reversal symmetry. As shown in Fig. 3(a), real-space orbital texture of the $\mathcal{P}$ sites demonstrates a homogeneous orbital angular momentum $\langle \hat{L}_{z,i}\rangle$ for the superfluid, where the atoms condense in the K point of the first Brillouin zone [inset of Fig. 5(a)], consistently with experimental observations [35]. The nonzero value of angular momentum in these phases is not surprising, since the p-orbital interactions, which are described by Eq. (2), favor the angular momentum order. For negative interaction $J/U_s = -1/6$, however, it is expected that $\langle \hat{L}_{z,i}\rangle = 0$ both in the superfluid [Fig. 3(b)] and Mott phases (MI$_{\text{I}}$ and MI$_{\text{III}}$) [Fig. 3(d)] to lower the energy of the system. But we do not observe Potts-nematic condensing at the M point [inset of Fig. 5(a)] for negative orbital-changing interactions, which was experimentally observed recently [34], and the reason may be due to the single-site solver used in our BDMFT approach.
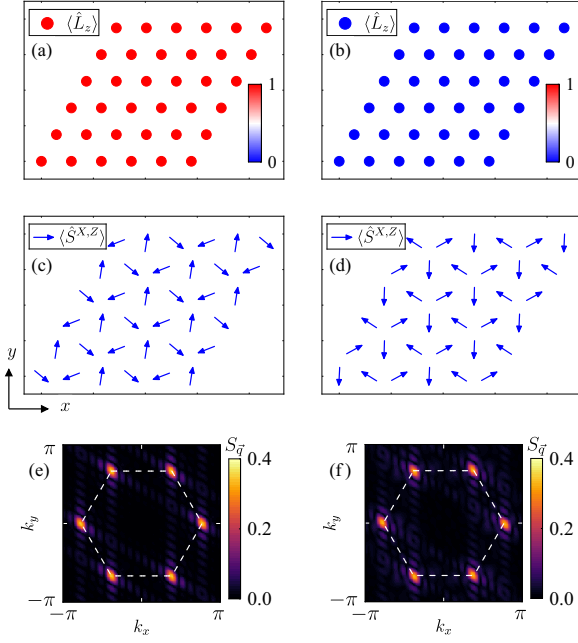
FIG. 3. Real-space distributions of orbital textures for the $\mathcal{P}$ sites with $J/U_s = 1/6$ (a), (c) and $J/U_s = -1/6$ (b), (d). (a), (b) real-space distributions of orbital angular momentum $\langle \hat{L}_{z,i} \rangle$ for the superfluid with $\mu/U_s = 0.3$ and $t_{sp}/U_s = 0.11$. The color of the dots represents the value of $\langle \hat{L}_{z,i} \rangle$. (c), (d) Real-space orbital textures for the Mott phases with filling $n = 1$ for $\mu/U_s = 0.3$ and $t_{sp}/U_s = 0.04$, where the blue arrows represent real-space distributions of local orbital order $\langle \hat{S}_i^{X,Z} \rangle$ for the $\mathcal{P}$ sites. (e), (f) The contour plots of the static orbital order structure factor $S_{\vec{q}}$ corresponding to (c) and (d).

Interestingly, we find a 120° in-plane orbital order in the Mott phase (MI$_I$) with filling $n = 1$ ($n_s = 1$ and $n_p = 1$) both for positive $J/U_s = 1/6$ [Fig. 3(c)] and negative interactions $J/U_s = -1/6$ [Fig. 3(d)], where 3×3 orbital textures of $\langle \hat{S}_i^{X,Z} \rangle$ appear for the $\mathcal{P}$ sites with $\langle \hat{L}_{z,i} \rangle = 0$ by respecting time-reversal symmetry. To understand the physical phenomena in the Mott insulating phase with filling $n = 1$, we need an effective orbital-exchange model for the deep Mott regime. The effective orbital-exchange Hamiltonian is obtained by considering the tunneling part as a perturbation to the full Hamiltonian [54–57]. In the
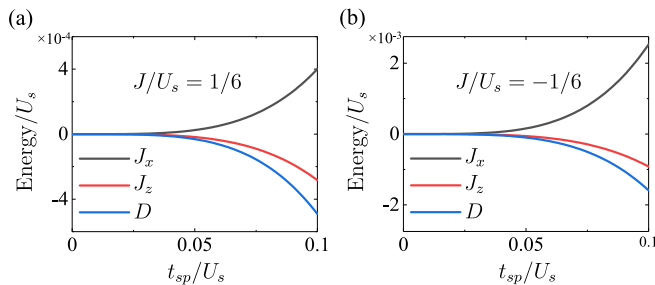

FIG. 4. Orbital-exchange interactions of the effective model as a function of the tunneling amplitude for $J/U_s = 1/6$ (a) and $J/U_s = -1/6$ (b). $J_x/J_z = -3$ and $D/J_z = \sqrt{3}$ for arbitrary hopping, as a result of rotational symmetry of the hexagonal lattice.

strong-coupling limit $t_{sp} \ll U_s$, we can use two projection operators $\hat{P}$ and $\hat{Q} = 1 - \hat{P}$ to divide the Hilbert space into two orthogonal subspaces. Here, $\hat{P}$ projects onto the subspace $\mathcal{H}_P$ with only one atom occupied per site, and $\hat{Q}$ projects onto the complementary subspace $\mathcal{H}_Q$ (see the Appendix B for details). For Hamiltonian $\hat{H}$, we divide it into two parts $\hat{H} = \hat{H}_t + \hat{H}_U$, where $\hat{H}_t$ describes tunneling terms and $\hat{H}_U$ describes interaction terms. The Schrödinger equation reads

$$\hat{H}|\psi\rangle = (\hat{H}_t + \hat{H}_U)(\hat{P} + \hat{Q})|\psi\rangle = E|\psi\rangle, \quad (10)$$

which leads to an effective Hamiltonian H_{eff} in the Mott phase with unit filling:

$$\hat{H}_{\text{eff}} = \hat{P}\hat{H}_t\hat{Q}\frac{1}{E - \hat{Q}\hat{H}\hat{Q}}\hat{Q}\hat{H}_t\hat{P}. \quad (11)$$

Because $E \sim t^2/U$, we obtain $\frac{1}{E - \hat{Q}\hat{H}\hat{Q}} \approx \frac{1}{-\hat{Q}\hat{H}_U\hat{Q} - \hat{Q}\hat{H}_t\hat{Q}}$. Using $\frac{1}{A-B} = \frac{1}{A}\sum_{n=0}^{\infty}(B\frac{1}{A})^n$, with $A = -\hat{Q}\hat{H}_U\hat{Q}$ and $B = \hat{Q}\hat{H}_t\hat{Q}$, we obtain the effective Hamiltonian:

$$\hat{H}_{\text{eff}} = \hat{P}\hat{H}_t\hat{Q}\frac{1}{-\hat{Q}\hat{H}_U\hat{Q}}\sum_{n=0}^{\infty}\left(\hat{Q}\hat{H}_t\hat{Q}\frac{1}{-\hat{Q}\hat{H}_U\hat{Q}}\right)^n\hat{Q}\hat{H}_t\hat{P}. \quad (12)$$

Since the system has two sets of sublattices, the second-order terms are then trivial. Taking a p-orbital atom as an example, it can tunnel to its neighboring $\mathcal{S}$ site as an s-orbital atom, and then the s-orbital atom can only tunnel back to the empty $\mathcal{P}$ site as a p-orbital atom. This is nothing but an onsite energy shift. Thus, it is not possible to generate effective interaction terms between the orbitals via second-order processes. Therefore, one must include fourth-order terms $\mathcal{O}(t^4/U^3)$, which give rise to the coupling between $\mathcal{P}$ sites to reach a nontrivial effective Hamiltonian. The effective orbital-exchange model is finally given by

$$\hat{H}_{\text{eff}} = \sum_{\langle ij \rangle} J_x \hat{S}_i^X \hat{S}_j^X + J_z \hat{S}_i^Z \hat{S}_j^Z + D(\hat{S}_i \times \hat{S}_j)_y, \quad (13)$$

where $\langle ij \rangle$ denotes the nearest-neighbor sites i and j of the $\mathcal{P}$ sublattice, and the Heisenberg exchange coupling terms $J_{x,z}$ and the Dzyaloshinskii-Moriya term D [58,59] are given in Appendix B. We find the disappearance of the Heisenberg exchange term J_y and the appearance of the Dzyaloshinskii-Moriya interaction D in the y direction in the effective exchange model, which is the underlying physics of the disappearance of orbital angular momentum with $\langle \hat{L}_{z,i} \rangle = 0$ for the Mott phase with filling $n = 1$. Instead, the Dzyaloshinskii-Moriya term competes with the normal exchange terms, and can induce coplanar orbital textures. We remark here that, in our system, mirror symmetry is actually broken as a result of the anisotropy of the p orbital. This is explained in more detail in Appendix C.

In Fig. 4, the coupling strengths are shown as a function of the tunneling amplitudes. Interestingly, we observe $J_x/J_z = -3$ and $D/J_z = \sqrt{3}$ for arbitrary hopping, as a result of rotational symmetry of the hexagonal lattice. Indeed, the interplay of the Dzyaloshinskii-Moriya and the normal exchange terms results in a 120° coplanar orbital order for the Mott insulating phase with $n = 1$, as shown in Figs. 3(c) and 3(d), where the blue arrows represent the real-space distribution of local
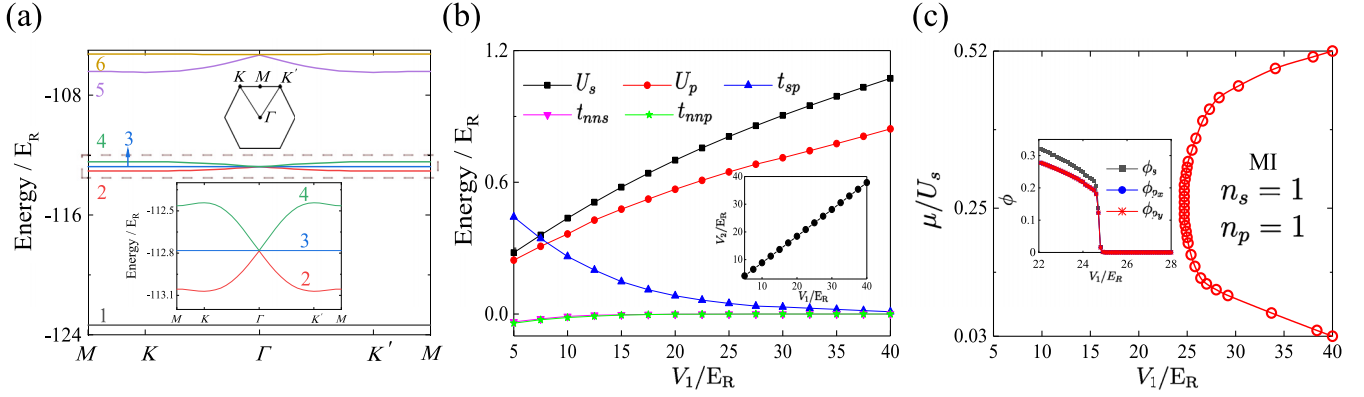
FIG. 5. (a) Band structure of an optical lattice with $V_1 = 15E_R$ and $V_2 = 13.6252E_R$, which have triple band crossings between the second, third, and fourth bands, indicating the s orbital being in resonance with the $p_{x,y}$ orbitals, where E_R is the recoil energy. Insets: Schematic diagram of the first Brillouin zone and high-symmetry points (top) and enlarged view of the second, third, and fourth bands (bottom). (b) Interaction and hopping parameters as a function of lattice depth V_1. Inset: s- and $p_{x,y}$-orbitals resonance for different lattice depths V_1 and V_2. (c) Phase diagram of the multiorbital bosonic atoms in a 2D hexagonal lattice, where the Hubbard parameters are obtained from band-structure simulations. Inset: Order parameters ϕ_v are shown as a function of V_1 for a fixed chemical potential $\mu/U_s = 0.25$, indicating the superfluid-Mott insulating phase transition.

orbital order $\langle \hat{S}_i^{X,Z} \rangle$ of the $\mathcal{P}$ sites. This phase is also characterized by the structure factor $S_{\vec{q}}$. As shown in Figs. 3(e) and 3(f), the structure factor exhibits six peaks at K and K' points.

B. Band-structure simulations and many-body phases

In the previous part, we study the multiorbital system with ideal Hubbard parameters. In this part, we investigate the robustness of quantum phases against Hubbard parameters, which can be obtained from band-structure simulations. In particular, we consider a two-dimensional bipartite hexagonal lattice potential:

$$V_{\text{hex}}(\mathbf{r}) = -V_1 \sum_{\substack{\alpha=1,-1 \\ \sigma=1,2,3}} \left[3 + e^{i\alpha(\mathbf{b}_\sigma \cdot \mathbf{r} - \frac{2\pi}{3})} \right]$$
$$-V_2 \sum_{\substack{\alpha=1,-1 \\ \sigma=1,2,3}} \left[3 + e^{i\alpha(\mathbf{b}_\sigma \cdot \mathbf{r} + \frac{2\pi}{3})} \right], \quad (14)$$

where V_1 and V_2 are the lattice depths of the two sets of lattices, and $\mathbf{b_1}$ and $\mathbf{b_2}$ are reciprocal-lattice vectors for the two-dimensional hexagonal lattice in the xy plane. In the third direction, we consider a strong laser field with $V_z = 50 E_R$ to freeze the motional degree of freedom, where E_R is the recoil energy. We choose $\mathbf{b_1} = \frac{4\pi}{\lambda}(\frac{3}{4}, -\frac{\sqrt{3}}{4})$, $\mathbf{b_2} = \frac{4\pi}{\lambda}(0, \frac{\sqrt{3}}{2})$, and $\mathbf{b_3} = \mathbf{b_1} + \mathbf{b_2}$ to generate a two-dimensional hexagonal lattice as shown in Fig. 1.

Experimentally, the potential difference between the $\mathcal{S}$ and $\mathcal{P}$ wells can be readily adjusted by tuning the ratio V_1/V_2, just as already done in the experiments [34,35,38]. In our case, we consider only three bands, i.e., second, third, and fourth bands, which can be isolated from other bands with atoms loading into these bands via band swapping technique [32,34,35]. Figure 5(a) shows the energy spectra of the six lowest-energy bands for $V_1 = 15 E_R$ and $V_2 = 13.6252 E_R$, based on a plane-wave expansion. Here, the second, third, and fourth bands

are isolated from other bands, and the corresponding orbitals are the s orbital in the shallow $\mathcal{S}$ sites and the $p_{x,y}$ orbitals in the deeper $\mathcal{P}$ sites, realizing a multiorbital system in a two-dimensional optical lattice.

For a sufficiently deep lattice, a tight-binding model can be utilized to describe the system, as shown in Eq. (1), based on the Wannier-function basis. The corresponding Hubbard parameters, such as interaction and hopping parameters, can be calculated using numerical methods. Here, we calculated the parameters of the Hubbard model using the maximally localized Wannier functions for composite bands [60–62], based on the software package [63]. In addition, we introduce the next-nearest-neighbor hopping terms $t_{\text{NN}s}$ and $t_{\text{NN}p}$, which are the nearest-neighbor hopping amplitudes within the same sublattice. Under the resonance of the s and $p_{x,y}$ orbitals by controlling the ratio V_1/V_2, the hopping amplitudes and interactions are shown as a function of V_1 in Fig. 5(b). Here, we take ^{87}Rb as an example, and choose the wavelength $\lambda = 1064$ nm, and s-wave scattering length $a_s = 100.4 a_0$ with a_0 being Bohr radius. We find that the next-nearest-neighbor hopping terms decrease quickly, approaching tiny values even for a moderate lattice depth.

Based on the Hubbard parameters obtained from band-structure simulations, we calculate the phase diagram of the multiorbital bosonic system in a two-dimensional hexagonal lattice. Generally, the next-nearest-neighbor hopping terms between the $p_{x,y}$ orbitals prefer a Potts-nematic superfluid with $\langle \hat{L}_{z,i} \rangle = 0$ by condensing atoms at the M point of the first Brillouin zone for the hexagonal lattice. However, the next-nearest-neighbor hopping is strongly suppressed for a moderately deep lattice, and, even for the lattice depth $V_1 = 5 E_R$, the physics is dominated by the nearest-neighbor hopping with developing chiral superfluid with $\langle \hat{L}_{z,i} \rangle \neq 0$. Upon increasing the lattice depth, the atoms localize, and a Mott insulator develops with a 120° coplanar orbital order for filling $n = 1$, as shown in Fig. 5(c).

IV. CONCLUSION

In summary, we study an experimentally related setup with ultracold bosons loaded into the s and $p_{x,y}$ bands of two-dimensional hexagonal optical lattices, and obtain zero-temperature quantum phases, based on bosonic dynamical mean-field theory. A rich phase diagram, including chiral superfluid, chiral Mott insulating, and time-reversal-even insulating phases, is found. In the strongly interacting regime, a fourth-order orbital-exchange model is derived, and a consistent description is found. To relate to experimental observations, we make band-structure calculations to obtain the Hubbard parameters, and resolve various quantum many-body phases, indicating the chance to observe these phases using current experimental techniques.

APPENDIX A: SITE-DEPENDENT ELEMENTS OF THE LATTICE GREEN'S FUNCTION

$$
\mathbf{G}_0^{-1}(i\omega_n) = \begin{pmatrix}
i\omega_n + \mu_s & 0 & -t_{\mathbf{e}_i}^{sp_x} & 0 & -t_{\mathbf{e}_i}^{sp_y} & 0 \\
0 & -i\omega_n + \mu_s & 0 & -t_{\mathbf{e}_i}^{sp_x} & 0 & -t_{\mathbf{e}_i}^{sp_y} \\
-t_{\mathbf{e}_i}^{sp_x} & 0 & i\omega_n + \mu_p & 0 & 0 & 0 \\
0 & -t_{\mathbf{e}_i}^{sp_x} & 0 & -i\omega_n + \mu_p & 0 & 0 \\
-t_{\mathbf{e}_i}^{sp_y} & 0 & 0 & 0 & i\omega_n + \mu_p & 0 \\
0 & -t_{\mathbf{e}_i}^{sp_y} & 0 & 0 & 0 & -i\omega_n + \mu_p
\end{pmatrix},
\tag{A1}
$$

where $t_{\mathbf{e}_i}^{sp_x} = x_i t_{sp}$ and $t_{\mathbf{e}_i}^{sp_y} = y_i t_{sp}$ with $\mathbf{e}_i = (x_i, y_i)$ (see main text).

APPENDIX B: EFFECTIVE ORBITAL-EXCHANGE MODEL

The fourth-order orbital-exchange model is given by

$$
\hat{H}_{\text{eff}} = \hat{P}\hat{H}_t\hat{Q}\frac{1}{-\hat{Q}\hat{H}_U\hat{Q}}\hat{Q}\hat{H}_t\hat{Q}\frac{1}{-\hat{Q}\hat{H}_U\hat{Q}}\hat{Q}\hat{H}_t\hat{Q}\frac{1}{-\hat{Q}\hat{H}_U\hat{Q}}\hat{Q}\hat{H}_t\hat{P}.
\tag{B1}
$$

In the tight-binding regime, we consider a three-site $(\mathcal{P}, \mathcal{S}, \mathcal{P})$ problem, and then the subspace $\mathcal{H}_P$, where all lattice sites are occupied with one atom, is

$$
\mathcal{H}_P : \{|p_x, s, p_x\rangle, |p_x, s, p_y\rangle, |p_y, s, p_x\rangle, |p_y, s, p_y\rangle\},
\tag{B2}
$$

where $|p_\sigma, s, p_{\sigma'}\rangle$ denotes the orbital state p_x or p_y in the $\mathcal{P}$ site and s in the $\mathcal{S}$ site. The subspace $\mathcal{H}_Q$, where one lattice site is occupied with two atoms, is

$$
\begin{aligned}
\mathcal{H}_Q : \{&|0, ss, p_x\rangle, |0, ss, p_y\rangle, |p_x, ss, 0\rangle, |p_y, ss, 0\rangle, |0, s, p_xp_x\rangle, |0, s, p_xp_y\rangle, |0, s, p_yp_y\rangle, |p_xp_x, s, 0\rangle, |p_xp_y, s, 0\rangle, \\
&|p_yp_y, s, 0\rangle, |p_x, 0, p_xp_x\rangle, |p_x, 0, p_xp_y\rangle, |p_x, 0, p_yp_y\rangle, |p_y, 0, p_xp_x\rangle, |p_y, 0, p_xp_y\rangle, |p_y, 0, p_yp_y\rangle, |p_xp_x, 0, p_x\rangle, \\
&|p_xp_y, 0, p_x\rangle, |p_yp_y, 0, p_x\rangle, |p_xp_x, 0, p_y\rangle, |p_xp_y, 0, p_y\rangle, |p_yp_y, 0, p_y\rangle\}.
\end{aligned}
\tag{B3}
$$

From these two subspaces, we can obtain the matrix form of $\hat{P}\hat{H}_t\hat{Q}$, $\hat{Q}\hat{H}_U\hat{Q}$, and $\hat{Q}\hat{H}_t\hat{Q}$. Equation (B1) yields the effective orbital-exchange model, which is described by Eq. (13). The three coupling strengths are given by

$$
J_x = \frac{6t_{sp}^4}{2U_s^2 U_{p_{xy}}} + \frac{6t_{sp}^4}{4U_s U_{p_{xy}}^2} + \frac{3t_{sp}^4}{16U_{p_{xy}}^3} + \frac{24Jt_{sp}^4}{-U_s^2\tilde{U}} + \frac{24Jt_{sp}^4(U_{p_x} + U_{p_y})}{-U_s\tilde{U}^2} + \frac{6t_{sp}^4(4J^3 + JU_{p_x}^2 + JU_{p_y}^2 + JU_{p_x}U_{p_y})}{-\tilde{U}^3},
$$

$$
\begin{aligned}
J_z = &\frac{2t_{sp}^4}{2U_s^2 U_{p_{xy}}} + \frac{2t_{sp}^4}{4U_s U_{p_{xy}}^2} + \frac{t_{sp}^4}{16U_{p_{xy}}^3} + \frac{t_{sp}^4(6U_{p_y} - 2U_{p_x})}{-U_s^2\tilde{U}} + \frac{t_{sp}^4(6U_{p_y}^2 - 2U_{p_x}^2 + 16J^2)}{-U_s\tilde{U}^2} \\
&+ \frac{t_{sp}^4((3U_{p_y}^3 - U_{p_x}^3)/2 + 2J^2 U_{p_x} + 10J^2 U_{p_y})}{-\tilde{U}^3},
\end{aligned}
$$

$$
\begin{aligned}
D = &\frac{\sqrt{3}t_{sp}^4(4J + U_{p_x} - 3U_{p_y})}{-U_s^2\tilde{U}} + \frac{\sqrt{3}t_{sp}^4(4JU_{p_x} + 4JU_{p_y} + U_{p_x}^2 - 3U_{p_y}^2 - 8J^2)}{-U_s\tilde{U}^2} \\
&+ \frac{\sqrt{3}t_{sp}^4(4J^3 + JU_{p_x}^2 + JU_{p_y}^2 - J^2 U_{p_x} - 5J^2 U_{p_y} + JU_{p_x}U_{p_y} + (U_{p_x}^3 - 3U_{p_y}^3)/4)}{-\tilde{U}^3},
\end{aligned}
\tag{B4}
$$

with $\tilde{U} = U_{p_x}U_{p_y} - 4J^2$.

TABLE I. A list of operators and their counterparts after undergoing symmetry operations.

$\hat{O}$	$I\hat{O}I^{-1}$	$M_{xy}\hat{O}M_{xy}^{-1}$	$M_{xz}\hat{O}M_{xz}^{-1}$	$M_{yz}\hat{O}M_{yz}^{-1}$
$\hat{b}_{i,p_x}$	$-\hat{b}_{i',p_x}$	$\hat{b}_{i',p_x}$	$\hat{b}_{i',p_x}$	$-\hat{b}_{i',p_x}$
$\hat{b}_{i,p_y}$	$-\hat{b}_{i',p_y}$	$\hat{b}_{i',p_y}$	$-\hat{b}_{i',p_y}$	$\hat{b}_{i',p_y}$
$\hat{S}_i^X$	$\hat{S}_{i'}^X$	$\hat{S}_{i'}^X$	$-\hat{S}_{i'}^X$	$-\hat{S}_{i'}^X$
$\hat{S}_i^Z$	$\hat{S}_{i'}^Z$	$\hat{S}_{i'}^Z$	$\hat{S}_{i'}^Z$	$\hat{S}_{i'}^Z$
$(\hat{S}_i \times \hat{S}_j)_y$	$(\hat{S}_{i'} \times \hat{S}_{j'})_y$	$(\hat{S}_{i'} \times \hat{S}_{j'})_y$	$-(\hat{S}_{i'} \times \hat{S}_{j'})_y$	$-(\hat{S}_{i'} \times \hat{S}_{j'})_y$

APPENDIX C: SYMMETRY ANALYSIS

We denote the spatial inversion operator as I and the mirror reflection operator as $M_{\alpha\beta=xy,xz,yz}$ with respect to the $\alpha\beta$ plane. Under the symmetry operations I and $M_{\alpha\beta}$, the p-orbital wave functions obtain a change due to its intrinsic anisotropy, so the operators $\hat{S}_i^{X,Z}$ and $(\hat{S}_i \times \hat{S}_j)_y$ are also changed (shown in Table I). We use the labels $i(j)$ and $i'(j')$ to represent the positions before and after the symmetry operation, respectively. The nonzero Dzyaloshinskii-Moriya interaction term in our model is a result of the break of mirror symmetry (M_{xz}, M_{yz}), which is essentially caused by the anisotropy of the p orbital.

[1] M. Lewenstein, A. Sanpera, V. Ahufinger, B. Damski, A. Sen(De), and U. Sen, Adv. Phys. **56**, 243 (2007).

[2] I. Bloch, J. Dalibard, and W. Zwerger, Rev. Mod. Phys. **80**, 885 (2008).

[3] O. Dutta, M. Gajda, P. Hauke, M. Lewenstein, D.-S. Lühmann, B. A. Malomed, T. Sowiński, and J. Zakrzewski, Rep. Prog. Phys. **78**, 066001 (2015).

[4] C. Gross and I. Bloch, Science **357**, 995 (2017).

[5] S. Sachdev, Nat. Phys. **4**, 173 (2008).

[6] F. D. M. Haldane, Rev. Mod. Phys. **89**, 040502 (2017).

[7] D. M. Weld, P. Medley, H. Miyake, D. Hucul, D. E. Pritchard, and W. Ketterle, Phys. Rev. Lett. **103**, 245301 (2009).

[8] B. Gadway, D. Pertot, R. Reimann, and D. Schneble, Phys. Rev. Lett. **105**, 045303 (2010).

[9] A. Mazurenko, C. S. Chiu, G. Ji, M. F. Parsons, M. Kanász-Nagy, R. Schmidt, F. Grusdt, E. Demler, D. Greif, and M. Greiner, Nature (London) **545**, 462 (2017).

[10] H. Sun, B. Yang, H.-Y. Wang, Z.-Y. Zhou, G.-X. Su, H.-N. Dai, Z.-S. Yuan, and J.-W. Pan, Nat. Phys. **17**, 990 (2021).

[11] M. Xu, L. Haldar Kendrick, A. Kale, Y. Gang, G. Ji, R. T. Scalettar, M. Lebrat, and M. Greiner, Nature (London) **620**, 971 (2023).

[12] C. Becker, P. Soltan-Panahi, J. Kronjäger, S. Dörscher, K. Bongs, and K. Sengstock, New J. Phys. **12**, 065025 (2010).

[13] J. Struck, C. Ölschläger, R. Le Targat, P. Soltan-Panahi, A. Eckardt, M. Lewenstein, P. Windpassinger, and K. Sengstock, Science **333**, 996 (2011).

[14] P. Soltan-Panahi, J. Struck, P. Hauke, A. Bick, W. Plenkers, G. Meineke, C. Becker, P. Windpassinger, M. Lewenstein, and K. Sengstock, Nat. Phys. **7**, 434 (2011).

[15] M. N. Kosch, L. Asteria, H. P. Zahn, K. Sengstock, and C. Weitenberg, Phys. Rev. Res. **4**, 043083 (2022).

[16] S. Taie, H. Ozawa, T. Ichinose, T. Nishio, and Y. Takahashi, Sci. Adv. **1**, e1500854 (2015).

[17] G.-B. Jo, J. Guzman, C. K. Thomas, P. Hosur, A. Vishwanath, and D. M. Stamper-Kurn, Phys. Rev. Lett. **108**, 045305 (2012).

[18] J. Vannimenus and G. Toulouse, J. Phys. C: Solid State Phys. **10**, L537 (1977).

[19] G. Semeghini, H. Levine, A. Keesling, S. Ebadi, T. T. Wang, D. Bluvstein, R. Verresen, H. Pichler, M. Kalinowski, R. Samajdar *et al.*, Science **374**, 1242 (2021).

[20] X. Li and W. V. Liu, Rep. Prog. Phys. **79**, 116401 (2016).

[21] M. Lewenstein and W. V. Liu, Nat. Phys. **7**, 101 (2011).

[22] W. V. Liu and C. Wu, Phys. Rev. A **74**, 013607 (2006).

[23] C. Wu, W. V. Liu, J. Moore, and S. Das Sarma, Phys. Rev. Lett. **97**, 190406 (2006).

[24] F. Hébert, Z. Cai, V. G. Rousseau, C. Wu, R. T. Scalettar, and G. G. Batrouni, Phys. Rev. B **87**, 224505 (2013).

[25] A. B. Kuklov, Phys. Rev. Lett. **97**, 110405 (2006).

[26] H. Tan, J. Han, W. Zheng, J. Yuan, and Y. Li, Phys. Rev. A **106**, 023315 (2022).

[27] Y. Li, J. Yuan, X. Zhou, and X. Li, Phys. Rev. Res. **3**, 033274 (2021).

[28] B. Liu, P. Zhang, H. Gao, and F. Li, Phys. Rev. Lett. **121**, 015303 (2018).

[29] P. Saugmann and J. Larson, New J. Phys. **22**, 023023 (2020).

[30] G. Wirth, M. Ölschläger, and A. Hemmerich, Nat. Phys. **7**, 147 (2011).

[31] M. Ölschläger, T. Kock, G. Wirth, A. Ewerbeck, C. M. Smith, and A. Hemmerich, New J. Phys. **15**, 083041 (2013).

[32] T. Kock, C. Hippler, A. Ewerbeck, and A. Hemmerich, J. Phys. B **49**, 042001 (2016).

[33] L. Niu, S. Jin, X. Chen, X. Li, and X. Zhou, Phys. Rev. Lett. **121**, 265301 (2018).

[34] S. Jin, W. Zhang, X. Guo, X. Chen, X. Zhou, and X. Li, Phys. Rev. Lett. **126**, 035301 (2021).

[35] X.-Q. Wang, G.-Q. Luo, J.-Y. Liu, W. V. Liu, A. Hemmerich, and Z.-F. Xu, Nature (London) **596**, 227 (2021).

[36] G.-H. Huang, Z.-F. Xu, and Z. Wu, Phys. Rev. Lett. **129**, 185301 (2022).

[37] C. Wu and S. Das Sarma, Phys. Rev. B **77**, 235107 (2008).

[38] X.-Q. Wang, G.-Q. Luo, J.-Y. Liu, G.-H. Huang, Z.-X. Li, C. Wu, A. Hemmerich, and Z.-F. Xu, arXiv:2211.05578 (2022).

[39] F. Pinheiro, General properties of the bosonic system in the p and in the d bands, in *Multi-Species Systems in Optical Lattices: From Orbital Physics in Excited Bands to Effects of Disorder* (Springer, New York, 2016), pp. 33–48.

[40] K. Byczuk and D. Vollhardt, Phys. Rev. B **77**, 235106 (2008).

[41] M. Snoek and W. Hofstetter, arXiv:1007.5223 (2010).

[42] M. Snoek, I. Titvinidze, C. Tőke, K. Byczuk, and W. Hofstetter, New J. Phys. **10**, 093008 (2008).

[43] R. W. Helmes, T. A. Costi, and A. Rosch, Phys. Rev. Lett. **100**, 056403 (2008).

[44] E. V. Gorelik, I. Titvinidze, W. Hofstetter, M. Snoek, and N. Blümer, Phys. Rev. Lett. **105**, 065301 (2010).

[45] Y. Li, J. Yuan, A. Hemmerich, and X. Li, Phys. Rev. Lett. **121**, 093401 (2018).

[46] R. Cao, J. Han, J. Wu, J. Yuan, L. He, and Y. Li, Phys. Rev. A **105**, 063308 (2022).

[47] A. Georges, G. Kotliar, W. Krauth, and M. J. Rozenberg, Rev. Mod. Phys. **68**, 13 (1996).

[48] A. Hubener, M. Snoek, and W. Hofstetter, Phys. Rev. B **80**, 245109 (2009).

[49] Y. Li, M. R. Bakhtiari, L. He, and W. Hofstetter, Phys. Rev. B **84**, 144411 (2011).

[50] W. S. Cole, S. Zhang, A. Paramekanti, and N. Trivedi, Phys. Rev. Lett. **109**, 085302 (2012).

[51] M. Hafez-Torbati, D. Bossini, F. B. Anders, and G. S. Uhrig, Phys. Rev. Res. **3**, 043232 (2021).

[52] H. Tan, J. Han, J. Yuan, and Y. Li, Phys. Rev. A **101**, 063611 (2020).

[53] J.-P. Martikainen and J. Larson, Phys. Rev. A **86**, 023611 (2012).

[54] L.-M. Duan, E. Demler, and M. D. Lukin, Phys. Rev. Lett. **91**, 090402 (2003).

[55] F. H. L. Essler, H. Frahm, F. Göhmann, A. Klümper, and V. E. Korepin, The Hubbard Hamiltonian and its symmetries, in *The One-Dimensional Hubbard Model* (Cambridge University, New York, 2005), pp. 20–49.

[56] F. Mila and K. P. Schmidt, Strong-coupling expansion and effective Hamiltonians, in *Introduction to Frustrated Magnetism: Materials, Experiments, Theory*, edited by C. Lacroix, P. Mendels, and F. Mila (Springer-Verlag, Berlin, 2011), pp. 537–559.

[57] F. Pinheiro, G. M. Bruun, J.-P. Martikainen, and J. Larson, Phys. Rev. Lett. **111**, 205302 (2013).

[58] I. Dzyaloshinsky, J. Phys. Chem. Solids **4**, 241 (1958).

[59] T. Moriya, Phys. Rev. **120**, 91 (1960).

[60] N. Marzari and D. Vanderbilt, Phys. Rev. B **56**, 12847 (1997).

[61] N. Marzari, A. A. Mostofi, J. R. Yates, I. Souza, and D. Vanderbilt, Rev. Mod. Phys. **84**, 1419 (2012).

[62] J. Ibañez-Azpiroz, A. Eiguren, A. Bergara, G. Pettini, and M. Modugno, Phys. Rev. A **87**, 011602(R) (2013).

[63] R. Walters, G. Cotugno, T. H. Johnson, S. R. Clark, and D. Jaksch, Phys. Rev. A **87**, 043613 (2013).